A speciation model linking the fate of carbon and hydrogen during coremagma ocean equilibration

Fabrice Gaillard, Valérie Malavergne, Mohamed Ali M.A. Bouhifd, Gregory Rogerie

▶ **To cite this version:**

Fabrice Gaillard, Valérie Malavergne, Mohamed Ali M.A. Bouhifd, Gregory Rogerie. A speciation model linking the fate of carbon and hydrogen during coremagma ocean equilibration. Earth and Planetary Science Letters, 2022, 577, pp.117266. 10.1016/j.epsl.2021.117266 . insu-03419023

HAL Id: insu-03419023
https://insu.hal.science/insu-03419023

Submitted on 8 Nov 2021

HAL is a multi-disciplinary open access archive for the deposit and dissemination of scientific research documents, whether they are published or not. The documents may come from teaching and research institutions in France or abroad, or from public or private research centers.

L'archive ouverte pluridisciplinaire **HAL**, est destinée au dépôt et à la diffusion de documents scientifiques de niveau recherche, publiés ou non, émanant des établissements d'enseignement et de recherche français ou étrangers, des laboratoires publics ou privés.

Fabrice Gaillard, Valérie Malavergne, Mohamed Ali Bouhifd, Gregory Rogerie. A speciation model linking the fate of carbon and hydrogen during core – magma ocean equilibration. Earth and Planetary Science Letters, Elsevier, 2022, 577, pp.117266. ⟨10.1016/j.epsl.2021.117266⟩

A speciation model linking the fate of carbon and hydrogen during core – magma ocean equilibration

Fabrice Gaillard[1], Valérie Malavergne[2], Mohamed Ali Bouhifd[3], Gregory Rogerie[1]

1- Université d'Orléans, CNRS, BRGM, ISTO, UMR 7327, F-45071, Orléans, France.
2- Université Paris Est-Marne La Vallée, Laboratoire des Géomatériaux et Environnement, Champs-sur-Marne, 77454 Cedex, France.
3- Laboratoire Magmas et Volcans, Université Clermont Auvergne, CNRS, IRD, OPGC, F-63000 Clermont-Ferrand, France.

Abstract.

The core – mantle differentiation in the magma ocean constitutes a major planetary event that involved two elements that are essential to life: carbon (C) and hydrogen (H). These two elements are conventionally classified as volatiles (ie. atmophile), but they can also evolve into being siderophile and lithophile at the extreme conditions found in planetary magma oceans. We report here a model for H and C species dissolved in silicate melts in equilibrium with iron-rich alloys under variable pressure, temperature and redox conditions. This speciation model is able to reconcile and reproduce a large body of experimental data on metal-silicate partitioning for H and C at carbon-saturation and in C-undersaturated systems. At low pressure, we conclude that the prevailing species in a silicate magma ocean are CO_2, CO, H_2O, H_2, whereas CH_4 appears to dominate at high pressure. These speciation changes explain recent experimental observations that (i) C evolves from being strongly siderophile at low pressure to moderately

siderophile at high pressure, and (ii) H is not siderophile at low pressure but becomes increasingly so as pressure rises. Moreover, it shows that H becomes increasingly siderophile as the total H content of the silicate melt and C-activity are lowered. Despite it offers a promising reconciliation of a large set of experimental and molecular dynamics observations, this model still suffers from large uncertainties when extrapolated to high pressure. In particular, endmember and mixing properties in both the silicate melt and the molten metal must be independently deciphered.

The enhanced CH_4 stability in the silicate melt at high pressure couples the fate of C and H in deep magma oceans. In such cases, the solubility of C in the basal ocean depends on the H-content and is higher than C-solubility at low pressure. This implies an increase in C activity as the ascending convective cells of the magma ocean, which may cause C saturation as graphite or diamond unless Fe-metal droplets, having a great C-solubility, are present in the shallow magma ocean. Under certain conditions, enhanced siderophile behaviour for H can lead via a runaway process to the desiccation of the magma ocean.

1. Introduction

Terrestrial planets evolved through early magma ocean stages (Rubie et al. 2015). These magma oceans were highly diverse on planetesimals, planetary embryos, and planets, implying increasingly extreme temperature and pressure conditions (*eg.* Li et al., 2016; Siebert et al., 2012). These molten stages are believed to provide an essential medium permitting planetary differentiation into a core, mantle, early crust and early atmosphere. Magma ocean is a general term embodying a silicate melt, with a varying fraction of silicate crystals, possibly coexisting

with molten metallic Fe-rich alloys, sulfide, carbide, graphite, diamond and a fluid phase. A major part of our understanding of the magma ocean stages on Earth is deduced from the interpretation of mantle depletion in variably siderophile elements through metal –silicate equilibria (*e.g*. Wade and Wood, 2005; Siebert et al., 2012; Rubie et al., 2015; Badro et al., 2015). The cause of mantle depletion of moderately siderophile elements with respect to chondritic abundances is generally attributed to the sequestration of the depleted elements into the core. Given the growing interest in the conditions defining habitable worlds, the distribution of C and H, two life-essential elements, during the magma ocean stage has been thrust into the scientific limelight (Okuchi, 1996; Hirschmann, 2012a; Sarafian et al., 2014; Li et al., 2016; Clesi et al., 2018; Malavergne et al., 2019; Greenwood et al., 2018; Grewal et al., 2019; Fischer et al., 2020; Li et al., 2020; Tagawa et al., 2021; Gaillard et al., 2021). At the pressure (P) – temperature (T) – redox conditions (oxygen fugacity fO_2) of modern magmatic and volcanic settings, C and H are considered as volatile elements or atmophile, ie. with a great affinity for the vapor phase (Iacono-Marziano et al., 2012). However, during the magma ocean stages, conditions were strongly reduced, and involved variable P-T conditions (1-60 GPa, 1500-4000°C), implying that some supposedly volatile elements could become magmatophile or siderophile and change the metal-silicate systematics (Ohtani et al., 2005; Hirschmann, 2012a; Gaillard et al., 2021). Wood et al. (2013), in their review paper, used a combination of thermodynamics, experimental data and isotopic constraints to predict a significant affinity of C for the metallic phase (of about 1 wt%) during metal-silicate equilibria taking place during the magma ocean stage. Okuchi (1996) reported experiments at high P and high-T (7 GPa, 1200-1500°C) revealing that H could be moderately siderophile. Capturing the behaviour of these elements during core formation is therefore not only important for deciphering the origin of a 5 to 10% density deficit in the Earth's core, but also because it may be a major stage in the construction of habitable worlds.

Recently, several research groups have produced experiments tackling the behaviour of C during metal silicate equilibration (eg. Wetzel et al., 2013; Dasgupta et al., 2013; Kadik et al., 2014; Stanley et al., 2014 ; Malavergne et al. 2019 ; Kuwahara et al. 2019; Fischer et al., 2020). These studies have reported equilibrium partitioning of C between molten Fe-rich metal and silicate melt at variable P, T, fO_2 and water (or H) contents. All these parameters affect the partitioning of C between metal and silicate. Using empirical linear relationships between the different variables (Eguchi and Dasgupta, 2018; Malavergne et al., 2019; Fisher et al., 2020), the dependencies of C partitioning on fO_2, T, P, water content and the amount of non-bridging oxygen per tetrahedron (NBO/T) have been fitted (NBO/T is an empirical parameter long known to control the solubility of carbon dioxide in molten silicates, eg. Iacono-Marziano et al., 2012). Most of these experimental studies also involved H (ie. often reported as water) and determined the H-content in the silicate melts, but so far, only three studies measured the partitioning of H between metal and silicate melts (Okuchi, 1996; Clesi et al., 2018; Malavergne et al., 2019) to 21 GPa, and recently, Tagawa et al (2021) indirectly estimated D^H at 30-60 GPa 3100-4600 K (using the phase proportions and the cell volume of FeHx et ε-FeOOH to get the H content in metals). These studies reported significant effects of P, T and fO_2 on H metal-silicate partitioning that are consistent with molecular dynamics calculations at extreme P and T (Zhang and Yin, 2012; Li et al. 2020, Yuan and Steinle-Neumann, 2020). Finally, empirical relationships have also been established to predict the molten metal – silicate liquid partitioning of H (Clesi et al., 2018; Malavergne et al., 2019; Tagawa et al 2021).

All these linear empirical models are phenomenological laws that do not consider the C-O-H chemical speciation in the silicate melts and their dependence on P, T and fO_2, which control H and C partition coefficients. These empirical approaches are interesting because they can provide input for a timely discussion generalizing and interpolating the experimental data points (eg. Fischer et al., 2020). However, equilibria related to the partition coefficient of an element

involving several species is, in principle, not constant and cannot be solved using a linear relationship. In our case for example, partitioning of C involves at least three species in the silicate melt: CO, CO_2, CH_4 (Armstrong et al., 2015), while the partitioning of H implies at least OH, H_2O, H_2 and CH_4 as dissolved species in the silicate melts. Here, we establish a thermochemical framework defining and linking the speciation of C and H in the silicate melt at the extreme conditions of the magma ocean. Even if this formalism is simple, it allows us to calculate with a unique formalism , the partitioning of both C and H between molten metal and silicate liquid, including C-undersaturated cases. This formalism shows that the current dataset, produced in various laboratories and covering a vast P-T-fO_2-volatile activity conditions, is consistent. However, high pressure solubility C-O-H data in metals and silicate melts , as well as some key thermodynamic parameters (such as compressibility) are missing rendering the extrapolation of this model to pressure greater than 30 GPa more challenging and uncertain. This approach paves the way for a broadened model to cover larger chemical systems (eg. to include other volatile elements such as O, S, and N and a vapour phase).

2. The database

Table 1 summarizes the 161 experiments used for the present thermochemical modelling. These experimental studies were conducted in the pressure range 1-21 GPa, in the temperature interval 1350 -2327 °C and with a fO_2 varying from -5.3 to +1.8 relative to the Iron-Wüstite (IW) redox buffer. The entire database (but Clesi et al, 2018) gives the C and H content of silicate melts at C-saturation. We have selected the experimental studies in which both H and C contents in the silicate melt were determined, thus the recent high-P work by Fischer et al. (2020), Fichtner et al. (2021) and Tagawa et al (2021) could not be used here (see the 2-next paragraphs). Clesi et al. (2018) did not measure the C-content in the silicate melts but C-contents in silicate melts at C-saturation under the P-T-fO_2-fH_2O conditions of their experiments is mostly provided by

other studies. The range of H-content in silicate melts (Table 1), converted into H_2O, is 0.009 (Armstrong et al. 2015) to 5 wt% (Kadik et al. 2014), which covers the expected conditions for any magma ocean. All experiments are C-saturated and provide the C-content of metals, but only two papers provide H concentrations in metals (20 experiments from Malavergne et al., 2019 and Clesi et al, 2018). Some experiments were excluded because the metal compositions were too rich in S (cut >1%) or Ni (cut at >10%), but this concerns only a four experiments in Li et al. (2015).

Table 1. Summary of the experimental studies considered. All experiments are C-saturated.

				SILICATE MELT		METAL	
Authors	P range (GPa)	T range (°C)	fO_2 range	C ppm	H ppm	C wt%	H ppm
Malavergne et al. 2019	1-15	1400-2300	-5.4 : -1.6	28-4100	277-1243	3.4-7	13-236
Clesi et al. 2018	5-21	1747-2427	-3.8 : -0.7	nd	402-1234	4.2-7.5	59-254
Eguchi & Dasgupta 2017	1-3	1425-1550	0.3 : 1.3	171 - 579	267-378	N.A.	N.A.
Li et al. 2017	1-2	1400-1550	-0.4 : 1.5	21 - 1388	100-656	N.A.	N.A.
Duncan et al., 2017	1	1600	1.6 : 1.8	900-2455	291-556	N.A.	N.A.
Li et al., 2016	1.5-8	1600-2200	-5.3 : -0.7	10-241	11-1172	3.03-5.7	N.A.
Stanley et al., 2014	1-3	1340-1617	-0.8 : 1.7	36-716	384-489	N.A.	N.A.
Wetzel et al., 2013	0.85 – 1	1500-1530	-1.1 : 1.6	199-1503	345-1698	7.6-8.3	N.A.
Armstrong et al., 2015*	1.2	1400	-1 : 1.5	8 - 864	10-1188*	6.2-7.7	N.A.
Li et al., 2015	3	1600	-4.7: -0.6	11 - 192	73 - 760	3.4-5.9	N.A.
Chi et al., 2014	1-3	1500-1800	-1 : - 0.4	9-129	210-2284	4.9-7.2	N.A.
Dasgupta et al., 2013	1-4	1600-2000	-1 : -0.8	11-93	321-1890	4.8-8.5	N.A.
Kadik et al. 2014	4	1550	-1.8: -3.4	4200-5800	2200-5500	N.A.	N.A.

* Only water (OH bonds), measured by FTIR, are given in this paper.

Figure 1 reports the C-content in silicate melts at C-saturation vs. fO_2, P and total H contents in the melts. For the experiments at fO_2<IW, these silicate melts are saturated in metal Fe containing 5-7 wt% C. Considering these metal-saturated experiments, we distinguished two groups of datapoints: a group with ca. <200 ppm C (low pressure, 1-5 GPa and low H content) and another one with C-content > 200 ppm (high pressure and/or high H-content). Such a large range of C contents dissolved in silicate melts at graphite-saturation (8-5800 ppm, Table 1,

Figure 1) may then reflect a range of C-speciation (CO_2, CO and CH_4, eg. Armstrong et al., 2015). But this large range has also cast doubt on the validity of some data. Recently, Fichtner et al (2021) argued that most of the data in table 1 and figure 1 are flawed due to a poor attainment of equilibrium. The point raised is that adding C as carbonate in the silicate starting material is a necessity to enhance equilibration rates since graphite-melt reactions are otherwise too sluggish. The datapoints of Fichtner et al. (2021) are indeed higher than most of the database (Figure 1a,1b) leading to the suspicion of unequilibrated C-contents in the silicate melts of most experimental data of table 1. In details, however, Fitchner et al. (2021) data indicates a range of C-content that is comparable to the studies of Malavergne et al. (2019) and Kadik et al. (2014) (see next paragraph). These three studies reported experiments that lasted ca. 10 minutes to 1 hour, whereas most other experiments of table 1, which are suspected of problem of equilibration, lasted a couple of hours: equilibration issues seem unlikely. It is also hardly conceivable that the C content of the glass would be far below equilibrium (and very low, eg <<200 ppm C), whereas the metal blobs spread in these glasses do show a high range of C-content (5-7 wt% C) that are consistent with C-saturation: if isolated metal blobs are C-saturated, the surrounding glass, connecting graphite to metal blobs, must also be equilibrated. Here, we consider that deviation of equilibration is a possibility for some data, but the generalisation of such a deviation is not justified by the existing experimental constraints taken as a whole: the range of C-content in figure 1 must reflect speciation effects.

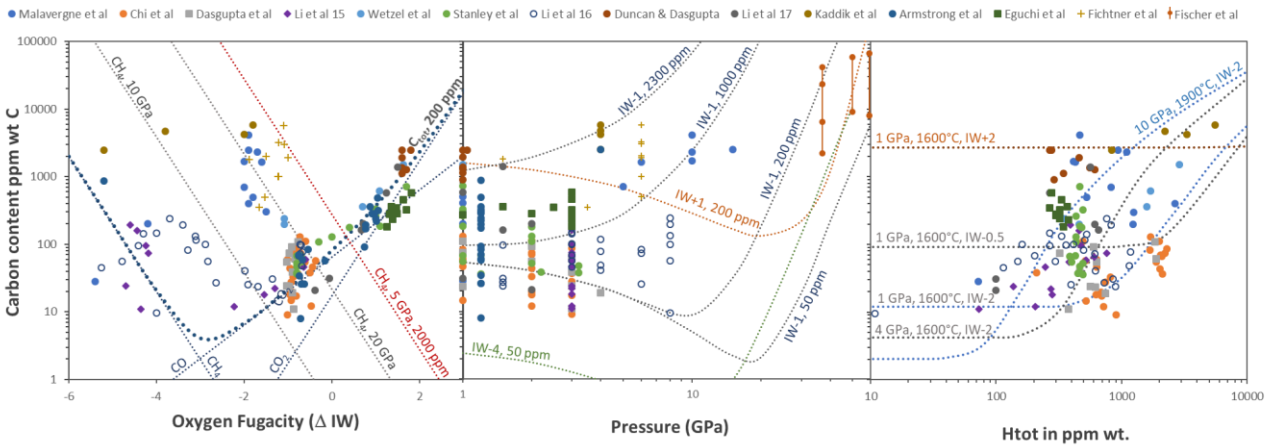

Figure 1: C content at C-saturation versus fO_2, P and H-content in the silicate melts. The database of Table 1 is shown here. The lines show calculations using the C-O-H speciation model for a range of P-T-H-fO_2 conditions that are representative of the conditions covered by the database. The data of Fichtner et al (2021) and Fischer et al (2020) are also shown though they have not been used to calibrate the speciation model. The data of Fichtner et al (2021) and Fischer et al (2020) can respectively be explained using the speciation model with ca. 1000-2000 ppm and ca. 50-200 ppm H_2O respectively.

As noticed before, the datapoints of Kadik et al. (2014) and some of Malavergne et al (2019) display both high C and high H contents (dissolved in the melt). This may reflect a higher proportion of CH_4. Regretfully, this assessment cannot be verified with the data of Fichtner et al (2021) since the H content of their samples is unknown. Fichtner et al. (2021) stated that their samples must be < 5000 ppm H_2O, which remains elevated, and they reported RAMAN spectra indicating dissolved CH_4. Elevated C content reported in Fichtner et al (2021) may then also reflect a significant amount of CH_4 in the glass. Another study, Fischer et al (2020), also reported high amounts of dissolved C, whereas the H contents of the glass are unknown. These data were collected at very high P and T (Figure 1b). Noteworthy, the RAMAN spectra of these samples revealed that CH_4 is the dominant dissolved form of C.

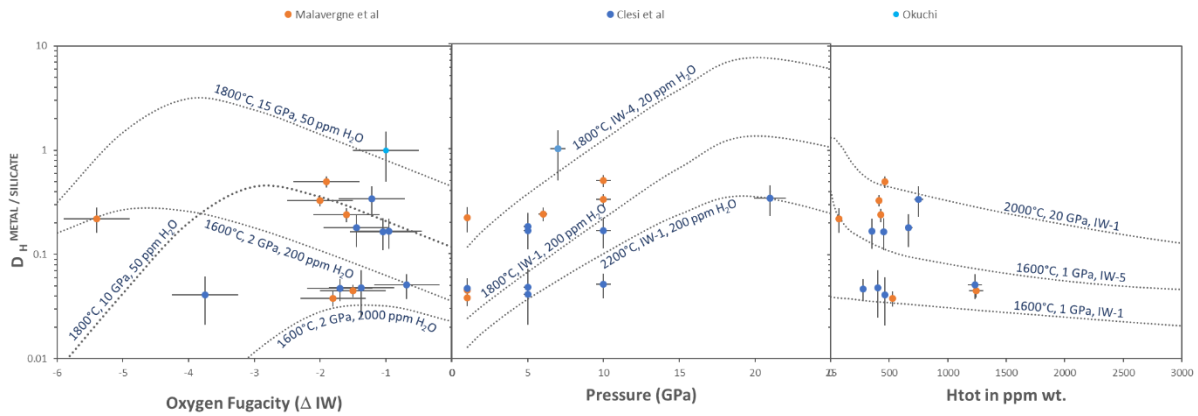

178

179 *Figure 2: H metal-silicate partitioning versus fO_2, P and H-content in the silicate melts. We*
180 *show here the data of Clesi et al (2018), Malavergne et al (2019) and Okuchi (1996). The lines*
181 *show calculations using the C-O-H speciation model for a range of P-T-H-fO_2 conditions that*
182 *are representative of the conditions covered by the database. The high-pressure (P>30 GPa)*
183 *MD data of Li et al (2020) and that experimental data of Tagawa et al (2021) are not shown*
184 *for sake of simplicity and because these were not used to calibrate our model.*

185 The 15 experimental H-partitioning data are shown in figure 2. Clesi et al (2018) and
186 Malavergne et al (2019) have reported metal-silicate partitioning data at C-saturation in the
187 pressure range 1-21 GPa, whereas Okuchi (1996) reported C-free data at 7 GPa. We can
188 distinguish C-saturated data being in the range D_H~ 0.03-0.6, whereas C-free data are in the
189 range D_H~1 or slightly higher. Using molecular dynamics calculations, Li et al (2020)
190 corroborated that H is siderophile in C-free conditions (ie. D_H>1) and they showed that D_H
191 increases with increasing P (to 20-135 GPa). The recent study of Tagawa et al (2021) also
192 confirms this result, though, we recall that the H-content in their Fe-alloys was indirectly
193 estimated. This positive P dependence has also been reported in C-saturated conditions (Clesi
194 et al., 2018; Malavergne et al., 2019) in the range 1-21 GPa (Figure 2).

195 To conclude on this brief review of available data on C and H metal-silicate partitioning, we
196 see that the partitioning systematics of both elements are linked: C partitioning (or C-content at

C-saturation) depends on H-contents, and H-partitioning is different in C-free and C-saturated conditions. In both cases, a significant effect of P has been noticed, rendering H more siderophile and C less siderophile. Below we present a simple thermodynamic framework that relates C and H speciation in silicate melts to changes in metal-silicate partition coefficients in P-T-fO_2-fH_2O parameter space.

3. Data Reduction

Each of the treated equilibria follows a law of mass action involving the constant of the reaction (K), in which the P and T dependences of the reaction's Gibbs free energy (ΔG_r) are approximated by the relationship:

$$\log K = -\frac{\Delta G_r}{RT} = \frac{A}{T} + B + C \times \frac{P}{T} \quad (1)$$

A, B and C are respectively related to the changes in enthalpy, entropy and volume associated with the reaction. Accordingly, in C-saturated charges, the C-content in metal (C^{METAL}) is defined as follows:

$C^{GRAPHITE} = C^{METAL}$ with $$\log K_2 = \log C^{METAL} + \log \gamma_C^{METAL} + \frac{A_2}{T} + B_2 + C_2 \times \frac{P}{T} \quad (2)$$

Here, γ_C^{METAL} stands for the activity coefficient of C in the Fe-metal (see supplementary section). At this stage, we consider γ_C^{METAL} to be P independent.

In the silicate melts of the C-O-H system, the total C-content is considered as being the sum of three species: CO_2, CO, and CH_4. Expressed in mass fraction, this yields:

$$C^{tot} = \frac{CO_2}{44} \times 12 + \frac{CO}{28} \times 12 + \frac{CH_4}{16} \times 12 \quad (3)$$

The total H content in the silicate melts is considered as being the sum of three species: H_2O, H_2, CH_4. Expressed as a mass fraction, this yields:

$$H^{tot} = \frac{H_2O}{18} \times 2 + \frac{H_2}{2} \times 2 + \frac{CH_4}{16} \times 4 \quad (4)$$

In most of the experimental conditions (Table 1), all H_2O is dissolved in the silicate melt, mostly as OH (Newcombe et al., 2017), but we computed these OH as H_2O equivalent (eg. Iacono-Marziano et al., 2012). This C-O-H speciation appears to be consistent with current state-of-the-art surveys (eg. Kadik et al., 2014; Armstrong et al., 2015, Malavergne et al., 2019; Dalou et al., 2019; Fischer et al. 2020). However, we admit that, in view of the limited number of studies on HP-HT speciation of C-O-H species in silicate melts, additional species may need to be considered in future models (*eg*. FeCO, CH_x or CO_x species; see Wetzel et al., 2013 ; Ardia et al., 2014 ; Kadik et al., 2014; Dalou et al., 2019; Solomatova et al., 2019).

The solubility of CO_2, CO and CH_4 are defined at C-saturation as:

$$C + O_2 = CO_2^{SILICATE} \quad (5)$$

$$C + ½\ O_2 = CO^{SILICATE} \quad (6)$$

$$C + 2\ H_2O^{SILICATE} = CH_4^{SILICATE} + O_2 \quad (7)$$

We considered CO_2 as an anionic species in the silicate $(CO_3)^{2-}$, implying that its solubility depends on oxygen O^{2-} activities in the melt in addition to fO_2. Iacono-Marziano et al. (2012) did use the NBO/T parameter as a proxy of O^{2-} activity to model carbonate solubility in mafic melts. This approach has also been considered in recent models on the C content at graphite saturation (Li et al. 2017). Accordingly, equilibria (5) and (6) are respectively modelled as:

$$\log K_5 = \log CO_2 + \frac{A_5}{T} + B_5 + C_5 \times \frac{P}{T} - \log fO_2 + D_5 \times \frac{nbo}{t} \quad (8)$$

$$\log K_6 = \log CO + \frac{A_6}{T} + B_6 + C_6 \times \frac{P}{T} - 0.5 \times \log fO_2 \quad (9)$$

239 Equilibria (7) is described as follows:

240 $$\log K_7 = \log CH_4 + \frac{A_7}{T} + B_7 + C_7 \times \frac{P}{T} + \log fO_2 + 2 \times \log H_2O \quad (10)$$

241 In equations (8-10), CO_2, CO, CH_4 and H_2O refer to the activity of these species in the silicate
242 melt. The activity of CO and CH_4 is equal to their mole fraction in the melt (assumed given the
243 low concentrations and the absence of proof of more complicated behaviour). The activity of
244 CO_2 depends on NBO, and that of H_2O in silicate melts has long been known to be proportional
245 to the square of the H_2O concentration (Newcombe et al., 2017 and references therein).
246 Accordingly, in all equilibria involving H_2O, its activity was computed as the square of the H_2O
247 melt content.

248 The total C content in silicate melts at C-saturation has been parameterized by merging eq. (3)
249 and eqs. (8-9-10). Since the activity of C, a_c, is 1, $\log a_C$ is null and is therefore absent in
250 equations (8) to (10), but C undersaturation in the metallic phase can be considered by adding
251 the term $-\log a_C$ to equations (8-10).

252 The H content in silicate melts is computed by merging eq. (4), eq. (7) and the following
253 equilibria:

254 $H_2^{SILICATE} + ½\ O_2 = H_2O^{SILICATE}$ (11)

255 The equilibrium constant for eq. (11) is written as:

256 $$\log K_{11} = \log H_2O - \log H_2 + \frac{A_{11}}{T} + B_{11} + C_{11} \times \frac{P}{T} - 0.5 \times \log fO_2 \quad (12)$$

257 H_2 refers here to the mole fraction of H_2 dissolved in the silicate melt (Hirschmann, 2012b).

258 The partitioning of H between silicate melt and metal has been calculated as:

259 $CH_4^{SILICATE} + ½\ O_2 = 4\ H^{METAL} + CO^{SILICATE}$ (13)

260 $$\log K_{13} = 4 \times \log \mathrm{H} + \log CO - \log CH_4 + \frac{A_{13}}{T} + B_{13} + C_{13} \times \frac{P}{T} - 0.5 \times \log fO_2 \quad (14)$$

261 Considering other stoichiometry (see Clesi et al., 2018) such as:

262 $H_2O = 2\,H + ½\,O_2$ or $H_2 = 2H$ (15)

263 these are all equivalent, since all the species involved are linked by equilibria (5-6-7-11) and
264 by the mass balance constraints (eqs. 3-4). This means that the partition coefficient of H can be
265 computed as:

266 $$D_H^{metal/silicate} = \frac{H^{metal}}{H^{silicate}} = \frac{H^{metal}}{\frac{CH_4^{silicate}}{16}\times 4 + \frac{H_2^{silicate}}{2}\times 2 + \frac{H_2O^{silicate}}{18}\times 2} \quad (16)$$

267 All thermodynamic constants involved in equations (8-10 and 14) are simultaneously adjusted
268 in order to reproduce the P-T-fO_2-H_2O dependences of the C-content in the silicate melt at C-
269 saturation and the metal silicate partitioning of H. In practice, we minimized the following sum:

270 $Soptim = f(\mathrm{H}^{\mathrm{SILICATE}}) + f(\mathrm{C}^{\mathrm{SILICATE}}) + f(\mathrm{H}^{\mathrm{METAL}}) + f(\mathrm{D_H}^{\mathrm{METAL}})$

271 with $f(H^{SILICATE}) = \frac{|H^{tot}_{mesured} - H^{tot}_{calculated}|}{\partial_{H^{tot}}}$, $f(C^{SILICATE}) = \frac{|C^{tot}_{mesured} - C^{tot}_{calculated}|}{\partial_{C^{tot}}}$,

272 $f(H^{METAL}) = \frac{|H^{METAL}_{mesured} - H^{METAL}_{calculated}|}{\partial_{H^{METAL}}}$ and $f(D_H{}^{METAL}) = \frac{|D_{H_{mesured}}^{METAL} - D_{H_{calculated}}^{METAL}|}{\partial_{D_H{}^{METAL}}}$

273 δ refers to the analytical error on the measured values as reported in the original study (we
274 considered 2σ). This specific effort was justified by the fact that reported errors greatly vary
275 from a study to another and from a sample to another.

276

277 **4. Predicting partitioning data in the parameter space**

278 4.1. Accuracy

In a simultaneous fitting process, all thermodynamic constants A_i, B_i, C_i appearing in equations (2, 8, 9, 10, 12, 14) have been parameterized in order to reproduce the P-T-fO_2 dependences of the C and H contents in a silicate melt and metals at C-saturation. The list of parameters is given in supplementary table S1. The results of the fit are given in figure 3 in terms of H and C-contents in a silicate melt at C-saturation. Recalculated data for H- and C-contents at C-saturation deviate on average by less than 33 % from the experimentally determined values (see Fig. 3; see also figure S1). Outlier datapoints concern a few experiments that conflict with the rest of the database, whereas P-T-H-fO_2-conditions are otherwise similar.

Uncertainties assessment on the A_i, B_i, C_i parameters adjusted using such non-linear multi-parameter fitting has no unique solution. We performed sensitivity tests on each adjusted parameter. This consists in varying each fitted parameter in order to probe its effect on the function *Soptim* (eq. 17, see figure S2). The upper and lower bounds for the A_i, B_i, C_i parameters were computed to match an increase of the Soptim function by 30% maximum (ie. an increase of the misfit by 30%, see figures S2). This 30% value corresponds to the mean accuracy of our model (see Fig. S1, where 1σ=15%). Quoted uncertainties are reported in table S1. Given the reported experimental uncertainties (in P, T, fO_2, H and C-contents) and the possible issue of calibration between different studies, we consider that the speciation model described here can reproduce the observed saturation and partitioning data reasonably well. The C and H contents and their uncertainties (a comprehensive error propagation formalism has been made available) can be calculated using our model in an online application http://calcul-isto.cnrs-orleans.fr/apps/silicate_melt/). Uncertainties in calculated C and H contents in silicate melts range from ca. 10% at pressure of 1 GPa-1600°C, 15-25 % at 10 GPa-1800°C, 20-50% at 30-2000°C GPa and 90-110% at 50 GPa, 3000°C. Uncertainties in calculated C and H contents in metal and D_C and D_H are propagated on the web-application through the various equations listed on section 3.

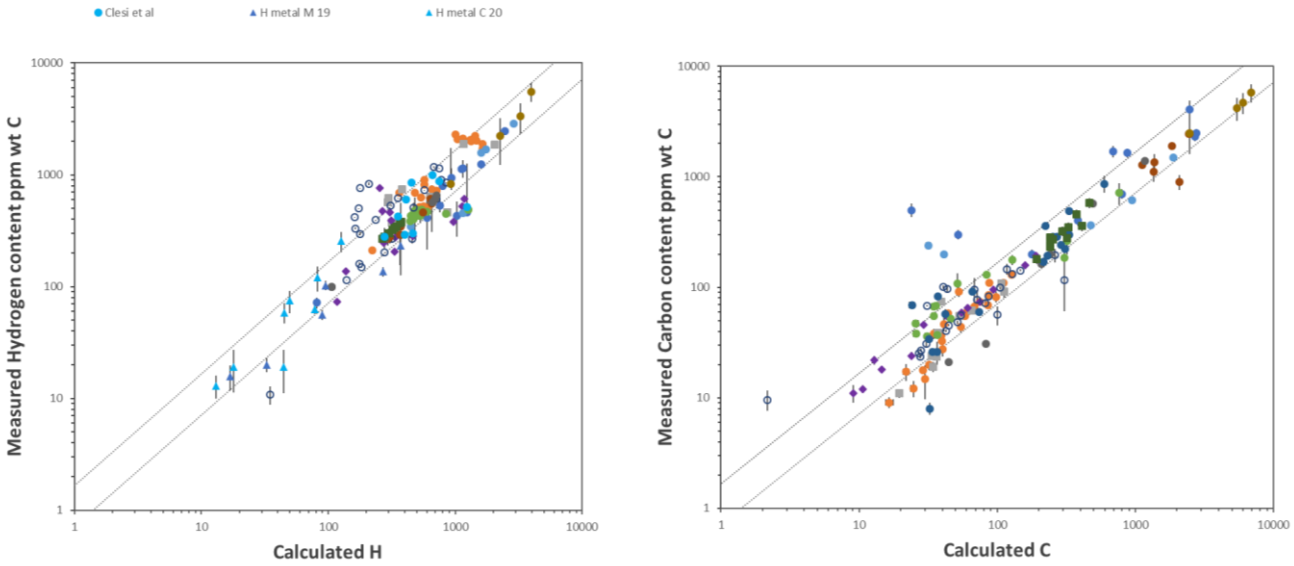

Figure 3: Observed vs predicted Carbon Content at C-saturation (CCCS) and H content in silicate melts and metals. The legend is similar to that used in figure 1 and the additional data are specified just above the left figure; these include the H-data of Clesi et al (2018) and Malavergne et al (2019). The 33% misfit lines are reported here. Outlier datapoints concern a few experiments that conflict with the rest of the database (P-T-H-fO_2-conditions being otherwise similar).

4.2. C-speciation in P-T-fO_2 parameter space.

Figure 1 illustrates the speciation methodology used to capture the C-content in silicate melt at C-saturation in metal. It shows the silicate melt C-contents at C-saturation vs. fO_2, vs. P and vs. total H content in the silicate melts taken from the entire experimental database; it also superimposes the calculated C-speciation at various fO_2-P-T-H_2O conditions. In figure 1a, the thick dotted blue line shows the C_{tot} (the sum of C as CO_2+CO+CH_4) at 2 GPa, 1500°C and for a H_2O content in the melt of 200 ppm. The fO_2 dependences of the fraction of C as CO_2, CO and CH_4 are shown with the thin dotted blue straight lines. We clearly see CO_2 being the

dominant form of C at high fO_2, CO at intermediate fO_2 and CH_4 at the lowest fO_2. The crossover CO_2-CO occurs at an fO_2 of about IW+1, as observed in specific experimental surveys (eg. Armstrong et al., 2015). The crossover CO-CH_4 occurs at ca. IW-3, but changing P or the H_2O content strongly modify this fO_2 values. For example, increasing P significantly increases the threshold fO_2, which becomes ca. IW-0.5 at 20 GPa. This P effect explains some of the Malavergne et al (2019) data. Increasing H_2O content also greatly increases the amount of CH_4, which can become the dominant form of dissolved C at 5 GPa-IW. This explains well the data of Kadik et al. (2014) that has so far been ignored in existing modelling (ie. Li et al., 2017; Eguchi et al., 2018; Fischer et al., 2020).

Figure 1b shows the P effect on C content at C-saturation. Calculated values bracket well the experimental data when considering a representative range of P-T-fO_2 conditions. These calculations also reveal two opposite trends. Moderately hydrated melts (≤200 ppm H_2O) show C-solubility that decreases with increasing P (to ca. 10-20 GPa), whereas hydrated melts show the opposite behaviour. C-decreasing with P is due to the fact that both CO and CO_2 have solubility at C-saturation that decrease with increasing P (Stanley et al., 2014; Li et al., 2017; Eguchi et al., 2018). For strongly hydrated samples, the C-solubility increases with P because our modelling implies that CH_4 is increasingly stabilized. This effect is data-driven since it results from the fitted values as described in section 3, but it must also reflect the volume change of the homogeneous reaction:

$$CO^{SILICATE} + 3\ H_2^{SILICATE} = CH_4^{SILICATE} + H_2O^{SILICATE} \quad (17)$$

$$CO_2^{SILICATE} + 4\ H_2^{SILICATE} = CH_4^{SILICATE} + 2H_2O^{SILICATE} \quad (18)$$

The volumes of the H_2O and CO_2 components and their P-T dependences are well-known and range, from 1 to 10 GPa, from 30 to 10 cc/mol and 34 to 22 cc/mol, respectively (ie. Gaillard et al., 2019). The volume of CH_4 and CO are, however, unknown. The solubility (ie. fluid-melt

equilibria) work of Ardia et al. (2014) and Armstrong et al. (2015) provides clues in the P range 1-5 GPa, that allowed us to estimate V_{CH4}~27 cc/mol and V_{CO}~22 cc/mol. The molar volume of H_2 is given in Hirschmann et al. (2012), V_{H2} = 11cc/mol. The volume changes of eq. (17) is ca. 2cc at ca. 1 GPa and may strongly evolve negative with increasing P, given the high compressibility of dissolved H_2O. We recall that the compressibility of CH_4 is unknown. We expect similar P-evolution for eq. (18) given the poor compressibility of CO_2 vs H_2O. We admit that independent and robust rationalization of the fact that CH_4 must dominate H-bearing systems at HP is needed. At this stage, our model, that is data driven, cannot accurately account for volume changes with P. Our sensitivity analyses make this clear (supplementary section). The relatively simple formalism we adopted is justified by its capacity to capture the C-solubility in the experimentally calibrated P-T-fO_2-fH_2O parameter space.

A noteworthy feature is visible in figure 1b with the P extrapolation of our model: C-content in H-poor silicate melts at C-saturation must first decrease with increasing P in the range 1-20 GPa (the domain where CO and CO_2 dominate) and then increase at higher P because of CH_4 formation. Note that the inflexion P depends on the H_2O content (ie. 20 GPa for 50 ppm H_2O, 10 GPa for 200 ppm H_2O and 5 GPa for 500 ppm H_2O, the latter is not shown in fig. 1b). We predict that above 35 GPa (though we calculate large uncertainties at such high P), C-content should be in the range 100-60,000 ppm, depending on the H_2O content of the silicate melts. In spite of the large uncertainties, this extrapolation is consistent with the data of Fischer et al. (2020). Fischer et al (2020) data cannot be used in our calibration database because the H-content in their silicate melts is unknown but they nevertheless reported RAMAN spectra showing that CH_4 is the only C-species detected in their sample. This give credence to our speciation model, but independent partial volume data and/or C-solubility experiments at high P are needed.

4.3.H-speciation and partitioning in P-T-fO_2 space

The H metal-silicate partition coefficient is also implicitly controlled by the C-O-H speciation and its P-T-fO_2 dependence. Figure 2 shows both experimental data and a range of calculation covering the relevant P-T-fO_2-fH_2O conditions. Figure 2a illustrates the fO_2 effect on H partitioning. This figure reveals two regimes:

- at oxidizing conditions, $D_H^{METAL/SILICATE}$ increases as fO_2 decreases, which reflects the following reaction $H_2O^{SILICATE} = 2\ H^{METAL} + ½\ O_2$
- at reducing conditions, $D_H^{METAL/SILICATE}$ increases as fO_2 decreases, which reflects the following reaction: $CH_4^{SILICATE} + O_2 = 4\ H^{METAL} + CO_2^{SILICATE}$

The reaction $H_2^{SILICATE} = 2\ H^{METAL}$ is necessarily operating but its effect (that should yield no fO_2 dependence) is weak in figure 2a.

The P effects are highlighted in figure 2b. Increasing P makes H more siderophile (as observed by Clesi et al, 2018 and Malavergne et al 2019), but this is strongly dependant on the fO_2, T and the total H-content (see also Fig.2c). These effects are consistent with the recent HP-HT experimental study of Tagawa et al (2021) and the molecular dynamics studies of Li et al. (2020) and Yuan and Steinle-Neumann (2020) conducted on C-free systems that reported increasing P makes H sensibly more siderophile. At ca. 20 GPa, however, the calculated D_H values reach a sort of plateau or an inflexion point, indicating the domain where CH_4 dominates in the silicate melt (see also fig. 1b for corresponding inflexion in the C-solubility vs P plot). Such an inflexion is obviously not described in the recent works cited above on C-free systems.

Figure 2c shows that lowering H-content in the silicate melt makes H more siderophile. This dependence of H-partitioning on H-content is also described in Li et al (2020) for a C-free system but not in other studies (Okuchi, 1998; Clesi et al., 2018; Malavergne et al., 2019). The effect of the H content is twofold: first, in reactions (13) and (15), ruling H-partitioning, 1 mole

394 of H-bearing species in the silicate melt reacts into 2 or 4 moles of H in the metal, a
395 stoichiometry implying that the partitioning changes with H-content; second, the relationship
396 between H_2O mole fraction in the silicate and activity of H_2O is a square function, which cancels
397 the stoichiometric effect for reaction 15 at low P (ie. when all H is H_2O). Figure 2c shows that
398 the effect of H-content is critical at high P and low fO_2 conditions, where CH_4 dominates. At
399 low P, where H_2O dominates the H-speciation, the effect of H-content is insignificant. All this
400 implies that the experiments must be collected in the expected range of H-content of the magma
401 ocean in order to be directly applicable. The range of H_2O content of the bulk silicate Earth
402 given in Marty (2012) (1000-3000 ppm H_2O, ca. 100-300 ppm H) and in Hirschmann (2018)
403 (620-800 ppm H_2O, ca. 60-80 ppm H) is the domain where small changes in the H-content of
404 the silicate melt is predicted to have an important effect on H metal-silicate partitioning. Most
405 current experimental data have been conducted above this range of H-content (Fig. 2c).

406 4.4.C-undersaturation at variable pressures

407 Calculations in fig 1-3 are conducted for C activity of unity (i.e., graphite/diamond-bearing
408 systems), however, in the absence of graphite/diamond, the activity of C is < 1 in metal, and
409 hence activity-composition models are required to quantify C partitioning between metal and
410 silicate. Such models must be confronted to experimental data at pressure. The experimental
411 work of Kuwahara et al. (2019) provided C-partitioning data at C-undersaturation.
412 Unfortunately, these experiments contain as much N as C, implying that the metal is a ternary
413 Fe-C-N with complex activity-composition relationships. Furthermore, these experiments are
414 massively contaminated with B (several wt % from the experimental assemblage). This makes
415 it difficult to use the Kuwahara et al. (2019) data as absolute C-partitioning data. Nevertheless,
416 this experimental work indicates that C tends to become less siderophile as the activity of C in
417 the metal is reduced. Note that the existing low P activity-composition relationships for C in
418 Fe-C (see supplementary section) implies that C should become more siderophile as C-activity

decreases (the activity coefficient of C in Fe-metal increases as C-activity increases). This effect is actually visible in figure 4b, where $D_C^{metal\text{-}silcate}$ is higher for C-undersaturated cases at P<10 GPa. At higher P, when CH_4 dominates, we notice an inversion of the effect of C-activity on $D_C^{metal\text{-}silcate}$. Here (Fig. 4b), the calculation is done for a fixed H_{tot} content (80 ppm H that is the Bulk Silicate Earth H-content after Hirschmann, 2018), and this H is essentially balanced between H_2O and CH_4. When CH_4 is involved, the total C-content does not only depend on a_C and fO_2, but it also depends on the fraction of H_2O (eq. 7). For a system containing more H_{tot}, the crossover, described in fig. 4b at 10 GPa, must occur at lower P. This simple analysis reveals that the effect of C-undersaturation on $D_C^{metal\text{-}silcate}$ is complex since it depends on P and H-contents in the silicate melt.

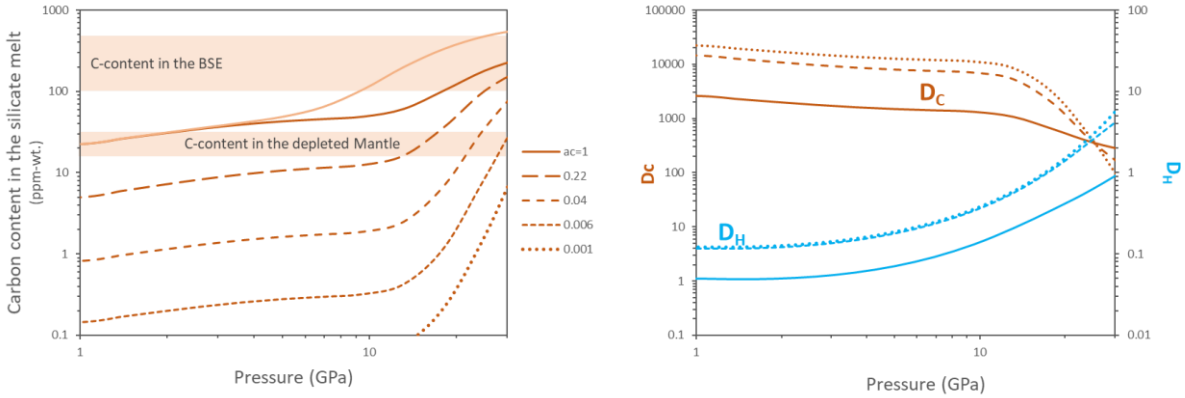

Figure 4: The effect of P and C-activity on the C-solubility in silicate melt and on the metal-silicate partitioning for C and H. As P increases from 1 to 30 GPa, T increases from 1600 to 2800°C. The H content is fixed to 80 ppm H (H-mantle after Hirschmann, 2018) in all curves but the pink one on the top of the left panel, which shows C-solubility for a silicate melt containing 160 ppm H.

The effect of C-activity on $D_H^{metal\text{-}silcate}$ is also addressed in Figure 4b, showing that H becomes increasingly siderophile as the metal C-activity is reduced. This is consistent with the results from the four available experimental studies (Okuchi, 1998; Clesi et al., 2018; Malavergne et al., 2019; Tagawa et al, 2021), indicating that H is more siderophile in C-free (D_H>1) than in

C-saturated systems (D_H<1). This is also consistent with the molecular dynamics data of Li et al. (2020) which demonstrate that partitioning of H between molten metal and silicate melt exceeds 10 at extreme P-T conditions (up to > 100 GPa and > 3000°C) in C-free systems. The driving force that makes H increasingly siderophile with C-undersaturation is captured by the following equilibrium, which dominates the metal-silicate partitioning of H at high P:

$$CH_4^{SILICATE} \rightarrow C + 4H^{METAL} \quad (18)$$

As the activity of C in metal is reduced, the above equilibrium is shifted to the right-hand side, making H more siderophile.

The behaviour of C-O-H species during metal – silicate equilibria under C-undersaturated conditions is currently under-constrained by experimental surveys. Whereas we are confident of the effect of C-undersaturation on D_H described here, its effect on D_C appears to be multiple and more difficult to capture. Experiments with C under-saturation conditions are essential to test the validity of the important conclusions reached at this stage.

5. Geochemical Implications for mantle - core differentiation on Earth

A series of calculations investigate the fate of H and C in the P-T-X parameter space permitted by our model. We limit our calculations to 30 GPa. Outside of this P-range, excessively large uncertainties prevent any sound discussion. These calculations nevertheless allow us to discuss the effect of variable values of C-activities and the effect of P. We consider two endmember cases:

(i) metal efficiently sinks and ponds at the base of the magma ocean (fig. 5, top-left side). The C and H partitioning at high-P high-T will control the activity of C and H in the entire magma ocean.

(ii) metal and silicate coexist all along the magma ocean vertical section (fig. 5, bottom-right side); in that case, C and H partition between metal and silicate at all depths.

Figure 4a shows the C-solubility in silicate melt vs. P (or depth) in a magma ocean. Variable values of C-activity are computed, whereas the H-content in the magma is fixed to 80 ppm H (Bulk Silicate Earth after Hirschmann, 2018; in addition, a sensitivity test shows the effect of doubling this amount of H). This means that we neglect H degassing as suggested by previous studies (Sossi et al., 2020; Gaillard et al., 2021). The C solubility increases with increasing P from ca. 20±5 ppm at 1 GPa to a maximum value of ca. 293±95 ppm at 30 GPa-2800°C. In the latter case, C is mostly as CH_4. Accordingly, most H (ie. 70 ppm H) is in the CH_4 form. The C content in the basal magma ocean is therefore controlled by the H availability. At low P, in contrast, most H occurs as H_2O (75 ppm H), most C occurs as dissolved CO (max. 13 ppm) and the remaining C occurs as CO_2 (4 ppm). A first conclusion must be highlighted here, the depth of the magma ocean controls its C content, implying that shallow magma oceans must have low C-contents (~ca. tens of ppm), whereas deep magma oceans enable high C-content (ca. >100 ppm C). At such high-P, the affinity of C for the metal is not as strong as at low P (Fig. 4b) implying that C assimilation by the core in large planet must weaken, whereas the core of small planets must massively take C. This point is consistent with the experimental model of Fischer et al (2020). The second conclusion is that convection-driven upward transfer of such C-rich basal magma ocean regions implies decompression-induced speciation changes, with C & H, shifting from CH_4-dominant to CO-H_2O dominant during ascent. Such a speciation change is not redox neutral and must consume oxygen (lowering the fO_2). In addition, as indicated in figure 4a, the solubility of C must decrease, implying that C saturation may be reached as the melt moves toward the surface of the magma ocean. This scenario is illustrated on the left part of figure 5, where a vertical gradient in C-solubility causes C-saturation in upwelling regions of the magma ocean, while downwelling regions must dissolve graphite or diamond. The C-

content in the basal silicate melt, where deep metal-silicate equilibration takes place, is controlled by the availability of H to form CH_4. In the case of figure 4, we recall that that the H content in the silicate melt is constant (80 ppm), and it corresponds to the H-content in the bulk silicate Earth. If this H content is doubled, it greatly impacts the C-solubility in the P domain where CH_4 dominates (fig. 4a). Marty (2012) reported much greater values (up to 290 ppm) than Hirschmann (2018) for the H-contents in the BSE. We therefore conclude that a large range of C-solubility in the basal magma ocean is possible (from ca. 200 to 1000 ppm) reflecting the uncertainties in H-content in the BSE (fig. 4a). In any case, we see that the calculated range of C-contents is comparable to the C-content of the depleted mantle in the P-range < 10 GPa and with C-content of the BSE (ie. Hirschmann, 2018; Marty, 2012) at P> 10 GPa.

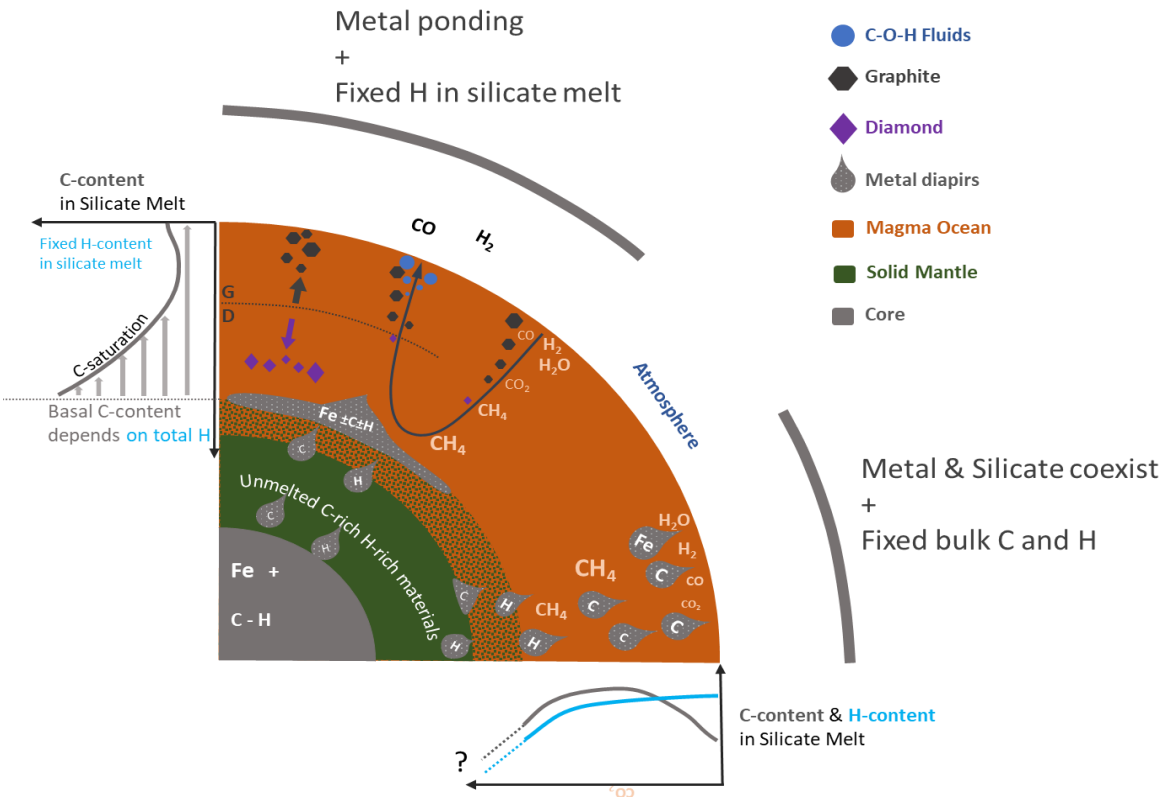

Figure 5: Diagram illustrating the two simulated magma ocean configurations, involving a basal layer of metal (top-left) and metal droplets being spread in the magma ocean (bottom-right). The top-left case is simulated in fig. 4, whereas the bottom-right one is shown in fig.6.

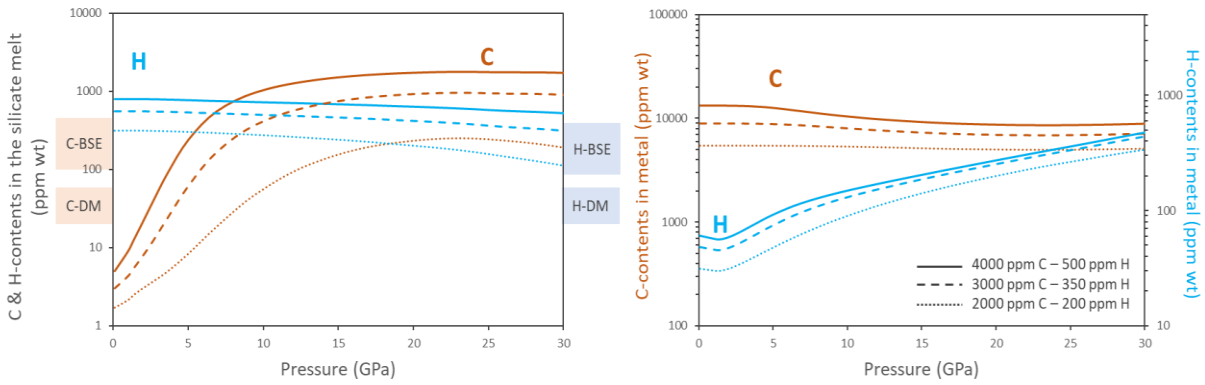

Figure 6: The fate of C & H in a magma ocean that contains Fe-metal at all depth. Here, we fixed the bulk C and H contents (in metal + silicate) as indicated in the legend. C solubility in the magma ocean increases with increasing P until a critical depth, where H becomes siderophile. Beyond this threshold P, we propose that the magma may get increasingly desiccated. P-T evolution similar to figure 4.

As illustrated in the right side of figure 5, if one considers that metal and silicate coexist all along the magma ocean vertical section, C-saturation is, in contrast, unlikely since the metal takes most C. We simulated in figure 6 such a case with fixed bulk C and H contents along the magma ocean profile (several runs were done with 4000-3000-2000 ppm C and 500-350-200 ppm H). Here, we focus on a somewhat simple, but increasingly popular model of accretion for planet Earth made up mainly of enstatite chondrites (eg. Javoy et al., 2010; Piani et al., 2020). Enstatite chondrites contain 4000 ppm C and 490 ppm H (Piani et al., 2020). We conducted calculations at a fixed fO_2 of IW-2 (no significant difference with simulations done at IW-4) for a set of P-T conditions similar to figure 4. At low pressure (ie. less than 5GPa), one sees that most C is sequestrated in the molten metal phase, leaving only a few tens of ppm C in the silicate melt. In contrast, H is mainly partitioned in the silicate melt. As P increases, C becomes less siderophile, reaching contents of ca. 200-1000 ppm-wt. in the silicate magma ocean, depending on the H content, at 20 GPa. This is because CH_4 becomes increasingly stable. In the meantime, H becomes increasingly siderophile. As P increases further, this can lead to the

dehydrogenation of the silicate melt, which may evolve dry at P>30 GPa, but our model does not allow calculations to be conducted at such pressure due to too large uncertainties. Whereas we are confident in the enhanced stability of CH_4 at high P, and the geochemical consequences we briefly expose here, reducing the uncertainties of predicted values is a necessity in order to quantitatively link chrondritic C-H abundances and the distribution of these elements during the magma ocean stages. In order to do so, we need independent constraints on C-O-H species compressibility and a-X relationships in a metal that become multicomponent and increasingly O-rich as pressure increase (eg. Tagawa et al., 2021)

6. Conclusions and perspectives

A growing body of experimental and molecular dynamics data have recently been produced in the literature on the partitioning of C and H during metal – silicate equilibria. Whereas these data originated from a number of laboratories, used different methods and produced different results, the modelling carried out here shows that all the data can be reconciled within the framework of a melt speciation model, involving the C-H-species H_2O, H_2, CO_2, CO, and CH_4 dissolved in a silicate melt. The dependence of the stability of these species on P, T and fO_2 can be related to previously determined values of H and C metal – silicate partition coefficients.

The use of this model allows us to distinguish two types of magma ocean: shallow and deep ones. In shallow magma oceans, C is strongly siderophile, while H is not siderophile. In deep magma oceans, C evolves to become less siderophile, while H becomes increasingly siderophile. The partitioning of H into metal depends on both P and C activity. In a C-poor, deep magma ocean, H incorporation into the core could lead to desiccation of the magma ocean.

Experimental and MD tests of this model are, however, needed since there are not enough constraints at this stage in certain regions of the parameter space (eg. low C-activity, high P

/low H content). Investigation of both C and H during partitioning are required since these are coupled through speciation relationships. This model is ultimately expected to evolve towards a multicomponent mixture taking into account all possible stoichiometric interactions between species in the C-H-O-N-S system (eg. Tsuno et al., 2018).

7. References

Ardia P., Hirschmann MM, Withers AC, Stanley BD, 2014. Solubility of CH4 in a synthetic basaltic melt, with applications to atmosphere–magma ocean–core partitioning of volatiles and to the evolution of the Martian atmosphere. Geochimica et Cosmochimica Acta 114, 52-71.

Armstrong, L.S., et al., 2015. The speciation of carbon, nitrogen, and water in magma oceans and its effect on volatile partitioning between major reservoirs of the Solar System rocky bodies. Geochim. Cosmochim. Acta 171, 283-302.

Badro, J., Brodholt, J.P., Piet, H., Siebert, J., Ryerson, F.J., 2015. Core formation and core composition from coupled geochemical and geophysical constraints. Proc. Natl Acad. Sci. USA 112, 12310–12314.

Chi, H., Dasgupta, R., Duncan, M.S., Shimizu, N., 2014. Partitioning of carbon between Fe-rich alloy melt and silicate melt in a magma ocean – implications for the abundances and origins of volatiles in Earth, Mars and Moon. Geochim. Cosmochim. Acta 139, 447–471.

Clesi, V., Bouhifd, M.A., Bolfan-Casanova, N., Manthilake, G., Schiavi, F., Raepsaet, C., Bureau, H., Khodja, H., Andrault, D., 2018. Low hydrogen contents in the cores of terrestrial planets. Sci. Adv. 4, e1701876.

567 Dalou C., Hirschmann M. M., Jacobsen S. D., Le Losq, C., 2019. Raman spectroscopy study
568 of C-O-H-N speciation in reduced basaltic glasses: implications for reduced planetary mantles.
569 Geochim. Cosmochim. Acta 265, 32–47.

570 Dasgupta, R., Chi, H., Nobumichi, S., Buono, A.S., Walker, D., 2013. Carbon solution and
571 partitioning between metallic and silicate melts in a shallow magma ocean: implications for the
572 origin and distribution of terrestrial carbon. Geochim. Cosmochim. Acta 102, 191–212.

573 Duncan, M. S., Dasgupta, R., Tsuno, K. (2017). Experimental determination of CO_2 content at
574 graphite saturation along a natural basalt-peridotite melt join: Implications for the fate of carbon
575 in terrestrial magma oceans. Earth Planet. Sci. Lett. 466, 115-128.

576 Eguchi, J., Dasgupta, R., 2017. CO_2 content of andesitic melts at graphite saturated upper
577 mantle conditions with implications for redox state of oceanic basalt source regions and
578 remobilization of reduced carbon from subducted eclogite. Contributions to Mineralogy and
579 Petrology 172, 12.

580 Eguchi, J., Dasgupta, R., 2018. A CO_2 solubility model for silicate melts from fluid saturation
581 to graphite or diamond saturation, Chem. Geol., 487, 23–38.

582 Fischer, R., et al., 2020. The carbon content of Earth and its core PNAS 117 (16) 8743-8749.

583 Fichtner C.E., et al., 2021. Carbon partitioning between metal and silicate melts during Earth
584 accretion. Earth and Planetary Science Letters, 554, 116659,
585 https://doi.org/10.1016/j.epsl.2020.116659

586 Gaillard, F., et al. (2019). The Link between the Physical and Chemical Properties of Carbon-
587 Bearing Melts and Their Application for Geophysical Imaging of Earth's Mantle. In B.
588 Orcutt, I. Daniel, & R. Dasgupta (Eds.), *Deep Carbon: Past to Present* (pp. 163-187).
589 *Cambridge: Cambridge University Press*.

590 Gaillard, F. et al. The Diverse Planetary Ingassing/Outgassing Paths Produced over Billions
591 of Years of Magmatic Activity. Space Sci. Rev. 217, 1‑54 (2021)

592 Greenwood, R.C., Barrat J-A, Miller M.F., et al., 2018. Oxygen isotopic evidence for accretion
593 of Earth's water before a high-energy Moon-forming giant impact. Science Advances 4 (3):
594 eaao5928.

595 Grewal, D.S., Dasgupta, R., Sun, C., Tsuno, K., Costin, G., 2019. Delivery of carbon, nitrogen,
596 and sulfur to the silicate Earth by a giant impact. Sci. Adv. 5, eaau3669.

597 Hirschmann, M.M., 2012a. Magma ocean influence on early atmosphere mass and composition.
598 Earth Planet. Sci. Lett. 341-344, 48–57.

599 Hirschmann, M.M., et al., 2012b. Solubility of molecular hydrogen in silicate melts and
600 consequences for volatile evolution of terrestrial planets. Earth and Planetary Science Letters
601 345-348 38–48.

602 Hirschmann, M.M., Comparative deep Earth volatile cycles: The case for C recycling from
603 exosphere/mantle fractionation of major (H2O, C, N) volatiles and from H2O/Ce, CO2/Ba,
604 and CO2/Nb exosphere ratios. *Earth Planet. Sci. Lett.* 502, 262–273 (2018)

605 Iacono-Marziano, G., Morizet, Y., Le-Trong, E., Gaillard, F., 2012. New experimental data and
606 semi-empirical parameterization of H_2O-CO_2 solubility in mafic melts. Geochim. Cosmochim.
607 Acta 97, 1-23.

608 Javoy, M., Kaminski, E., Guyot, F., Andrault, D., Sanloup, C., Moreira, M., Labrosse, S.,
609 Jambon, A., Agrinier, P., Davaille, A., Jaupart, C., 2010. The chemical composition of the
610 Earth: enstatite chondrite models. Earth Planet. Sci. Lett. 293, 259–268.

611 Kadik, A.A., Koltashev, V.V., Kryukova, E.B., Plotnichenko, V.G., Tsekhonya, T.I.,
612 Kononkova, N.N., 2014. Solution behavior of C-O-H volatiles in FeO-Na_2O-Al_2O_3-SiO_2 melts
613 in equilibrium with liquid iron and graphite at 4 GPa and 1550 °C. Geochem. Int. 52, 707–725.

614 Kuwahara, H., Itoh, S., Nakada, R., Irifune, T., 2019. The effects of carbon concentration and
615 silicate composition on the metal–silicate partitioning of carbon in a shallow magma ocean.
616 Geophysical research letters. doi: 10.1029/2019GL084254.

617 Li, Y., Dasgupta, R., Tsuno, K**.**, 2015. The effects of sulfur, silicon, water, and oxygen fugacity
618 on carbon solubility and partitioning in Fe-rich alloy melt-silicate melt systems at 3 GPa and
619 1600 °C – Implications for core-mantle differentiation and degassing of magma oceans and
620 reduced planetary mantles. Earth Planet. Sci. Lett. 415, 54-66.

621 Li, Y., Dasgupta, R., Tsuno, K., Monteleone, B., Shimizu, N., 2016. Carbon and sulfur budget
622 of the silicate Earth explained by accretion of differentiated planetary embryos. Nat. Geosci. 9,
623 781–785.

624 Li, Y., Dasgupta, R., Tsuno, K., 2017. Carbon contents in reduced basalts at graphite saturation:
625 Implications for the degassing of Mars, Mercury, and the Moon. Journal of Geophysical
626 Research - Planets 122, doi:10.1002/2017JE005289.

627 Li, Y., Vočadlo, L., Sun, T., Brodholt, J.P., 2020. The Earth's core as a reservoir of water. Nat.
628 Geosci. 13, 453–458.

629 Malavergne, V. et al., 2019. Experimental constraints on the fate of H and C during planetary
630 core–mantle differentiation. Implications for the Earth. Icarus 321, 473–485.

631 Marty, B., 2012. The origins and concentrations of water, carbon, nitrogen and noble gases on
632 Earth. Earth Planet. Sci. Lett. 313-314, 56-66.

633 Newcombe, M.E., Brett, A., Beckett, J.R., Baker, M.B., Newman, S., Guan, Y., Eiler, J.M. and
634 Stolper, E.M., 2017. Solubility of water in lunar basalt at low pH_2O. Geochim. Cosmochim.
635 Acta 200, 330–352.

636 Okuchi, T., 1996. Hydrogen Partitioning into Molten Iron at High Pressure: Implications for
637 Earth's Core. Science 278, 1781-1784.

638 Ohtani, E., Hirao, N., Kondo, T., Ito, M., Kikegawa, T., 2005. Iron–water reaction at high
639 pressure and temperature, and hydrogen transport into the core. Phys. Chem. Miner. 32, 77–82.

640 Piani, L., et al., 2020. Earth's water may have been inherited from material similar to enstatite
641 chondrite meteorites. Science 369, 1110-1113.

642 Rubie, D.C., et al., 2015. Accretion and differentiation of the terrestrial planets with
643 implications for the compositions of early-formed Solar System bodies and accretion of water.
644 Icarus 248, 89–108.

645 Sarafian, A.R., Nielsen, S.G., Marschall, H.R., et al., 2014. Early accretion of water in the inner
646 solar system from a carbonaceous chondrite–like source. Science 346, 623–626.

647 Siebert, J., Badro, J., Antonangeli, D., Ryerson, F.J., 2012. Metal-silicate partitioning of Ni and
648 Co in a deep magma ocean, Earth Planet. Sci. Lett. 321, 189-197.

649 Solomatova, N. V., Caracas, R., Manning, C.E., 2019. Carbon sequestration during core
650 formation implied by complex carbon polymerization, Nature Communications, 10(1), 789,
651 doi:10.1038/s41467-019-08742-9.

652 Stanley, B.D., Hirschmann, M.M., Withers, A.C., 2014. Solubility of C-O-H volatiles in
653 graphite-saturated martian basalts. Geochim. Cosmochim. Acta 129, 54–76.

654 Tagawa, S., Sakamoto, N., Hirose, K. *et al.* Experimental evidence for hydrogen incorporation
655 into Earth's core. *Nat Commun* **12,** 2588 (2021). https://doi.org/10.1038/s41467-021-22035-0

Tsuno, K., Grewal, D.S., R. Dasgupta, R., 2018. Core-mantle fractionation of carbon in Earth and Mars: The effects of sulfur. Geochim. Cosmochim. Acta 238, 477–495.

Wade, J, Wood, B.J., 2005. Core formation and the oxidation state of the Earth. Earth Planet. Sci. Lett. 236 78-95.

Wetzel, D.T., Rutherford, M.J., Jacobsen, S.D., Hauri, E.H., Saal, A.E., 2013. Degassing of reduced carbon from planetary basalts. Proc. Natl. Acad. Sci. USA 110, 8010–8013.

Wood, B.J., Li, J., Shahar, A., 2013. Carbon in the core: Its influence on the properties of core and mantle. Reviews in Mineralogy & Geochemistry, 75, 231-250.

Yuan, L., Steinle-Neumann, G., 2020. Strong sequestration of hydrogen into the Earth's core during planetary differentiation. Geophysical Research Letters, 47, e2020GL088303.

Zhang, Y., Yin, Q. Z., 2012. Carbon and other light element contents in the Earth's core based on first-principles molecular dynamics. PNAS 109, 16579-16583.

8. Acknowledgment

This research is supported by the GASTON project (ANR-18-CE31-0021). G.R. is supported by the VOLTAIRE project (ANR-10-LABX-100-01). We acknowledge the careful reviews by M Hirschmann and Paolo Sossi.

675 ## 9. Supplementary information

676

677 **H & C activity coefficient in metal**

678 The behaviour of H in metals is not thought to be ideal but its activity coefficient follows the
679 empirical relationships given in Lob et al (2011):

680 $$\log \gamma_H = 0.169 \times C^{METAL} - 0.2516 \quad (17)$$

681 Where C^{metal} stands for the mass fraction of C in metal. Activity-composition relationships for
682 C in metals have been defined in the metallurgy literature (eg. Wang et al. 1991). These are
683 used with the calculations for C-undersaturated systems below (see section 4.4). The presence
684 of <20% Ni is not considered to affect the activity of H as shown by previous thermodynamic
685 analyses of the 1-atm database (Jiang et al., 2011). We must specify at this stage that the non-
686 ideality laws for H and C in the metal as suggested from 1-atm studies have not yet been verified
687 by HP data. We suggest that specific HP experimental studies be devoted to this purpose (eg.
688 Li et al., 2016 for C-S interactions in metals).

689

690 **Regressed parameters**

691 Regressed parameters and their uncertainties are shown in table S1. These constants can be used
692 to compute the log K of each reactions as follows:

693 $$\log K = -\frac{\Delta G_r}{RT} = \frac{A}{T} + B + C \times \frac{P}{T} + D \times NBO$$

694 In table S1, the A terms must be multiplied by 1000. Note that the C terms is in some cases
695 modified as $C^{mod} = C + C' \times P/T$ in order to allow the volume change of the reaction to change

with P and T. In most of these cases, the uncertainties are very large underlining the need of getting robust compressibility data for C-O-H species in silicate melts.

Our procedure for getting uncertainties imply that these are not symmetrical so we give in table S1 the lower and upper bound values for each fitted value.

Table S1: Regressed parameters and their upper and lower bounds. Units allow the log K of each reaction to be calculated in molar ratios.

Reaction	Constant	Best fit	Bounds
	A2	-0.487	-0.52 / -0.41
	B2	1.022	1.11 / 0.85
C metal	**C2**	-0.006	-0.007 / -0.005
	A5	-8.794	-9.3 / -8.5
	B5	-0.054	-0.35 / 0.1
	C5	-0.201	-0.6 / 0.05
	C5'	9.512	2 / 21
CO2	**D5**	0.784	0.57 / 0.9
	A6	-1.658	-1.83 / -1.53
	B6	-2.220	-2.31 / -2.15
CO	**C6**	-0.287	-0.38 / -0.2
	A7	-9.760	-9.96 / -9.62
	B7	0.019	-0.07 / 0.081
	C7	0.441	0.406 / 0.465
CH4	**C7'**	-6.382	-16.8 / 0.9

	A11	-6.867	-20 / -6
	B11	-0.165	-4 / 0.25
H2	**C11**	-0.638	-4 / -0.3
	A13	15.470	12.8 / 16.6
	B13	0.612	-0.7 / 1.2
	C13	0.012	-0.35 / 0.15
H metal	**C13'**	7.085	-2 / 15

704

705 The online calculation tools use the numbers provided in table S1 to calculate the various
706 equilibria. The uncertainty propagations use an average error (lower bound – upper bound
707 divided by 2).

708 The ability of our model to reproduce the experimental observations has been quantified in
709 figure S1, which shown the distribution of residues expressed as deviation per data, in fraction,
710 expressed as follows:

711 Deviation = (observation – computed) / observation

712 A value of 1 means that the misfit is 100 %. The distribution of residues (fig. S1) indicates a
713 one sigma value of 0.15 (15 %), which explains the 30 % uncertainties (2 sigma) announced in
714 section 4.1.

715

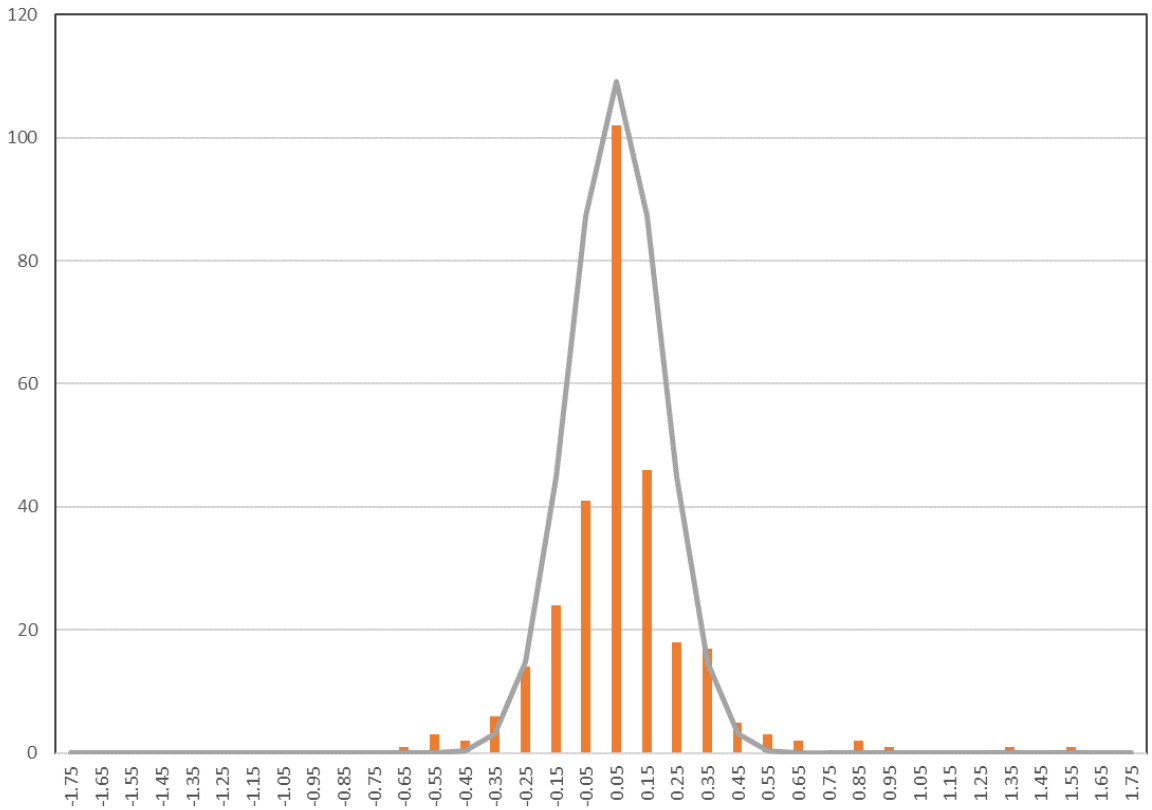

Figure S1: Frequency diagram showing the distribution of misfit per data. The horizontal scale is expressed as fraction of the value to fit. In practice, this must be read as more than 100 experimental observations are reproduced to within 5%. In grey is shown a log-normal curve calculated for a 1-sigma of 0.15.

Figure S2 illustrates the sensitivity tests for some of the regressed parameters. The values of the Soptim function (residues normalized to experimental uncertainties) vary as the regressed parameters are changed, with a minimum centred on the regressed values. In most cases, the error a non-symmetrical. We considered that values of the Soptim function below 180,000 (30% variation relative to the minimum) correspond to the acceptable range for the regressed parameters.

727

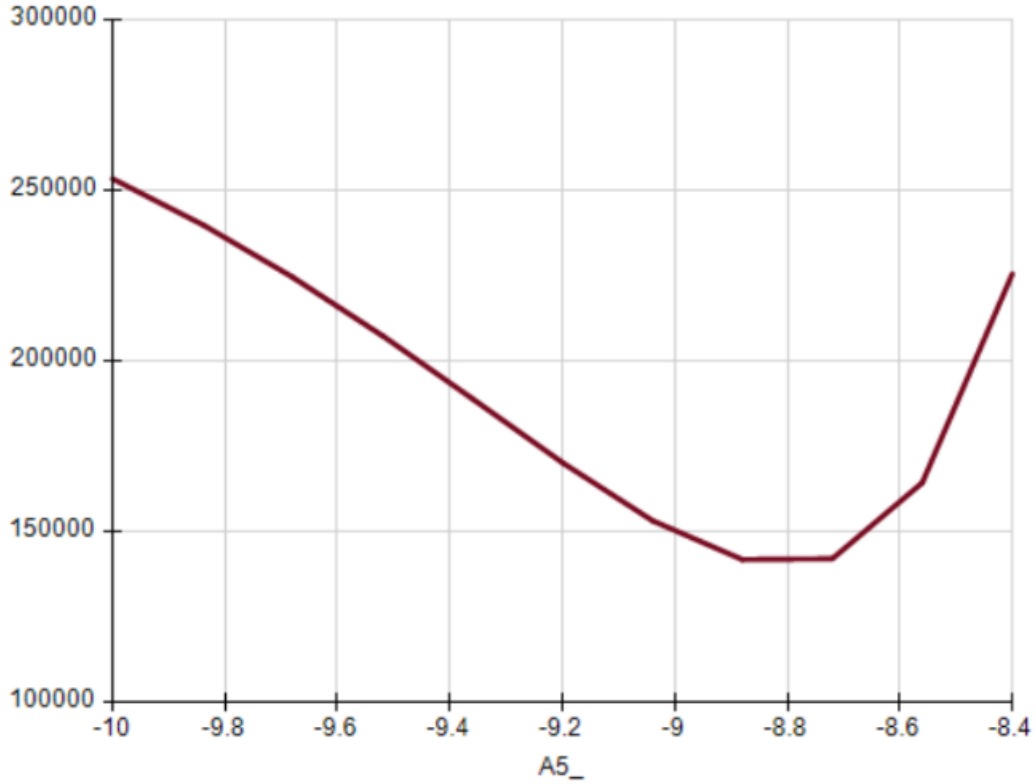
300000
250000
200000
150000
100000
-10
-9.8
-9.6
-9.4
-9.2
-9
-8.8
-8.6
-8.4
A5_

728

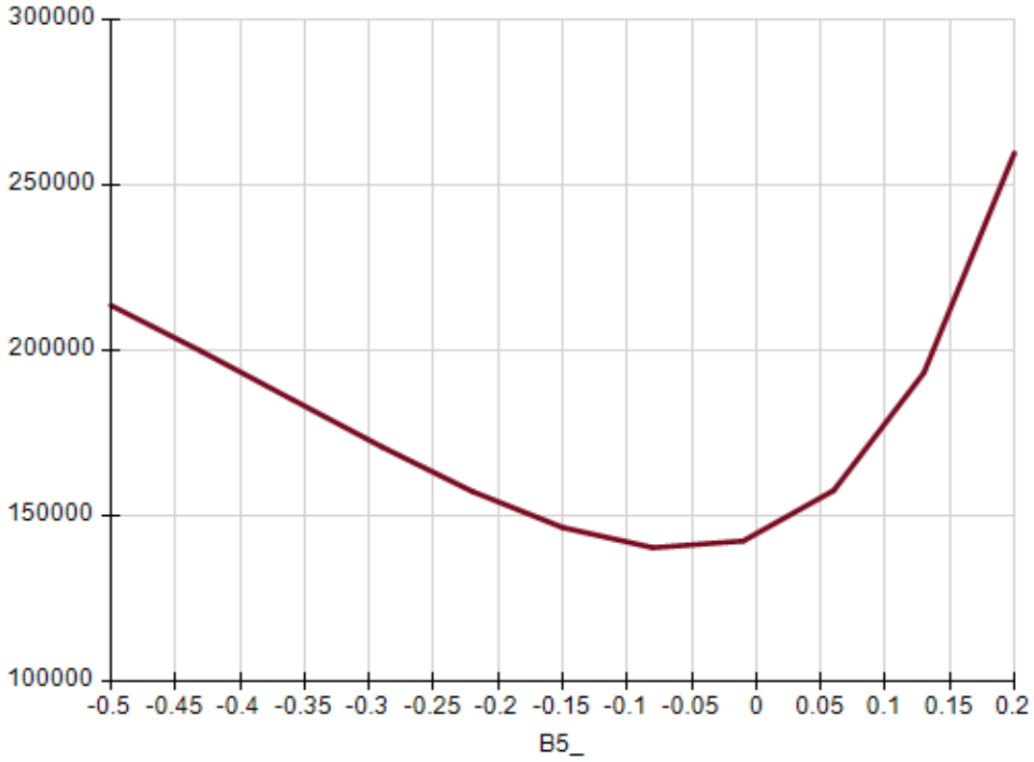
300000
250000
200000
150000
100000
-0.5
-0.45
-0.4
-0.35
-0.3
-0.25
-0.2
-0.15
-0.1
-0.05
0
0.05
0.1
0.15
0.2
B5_

729

730

731

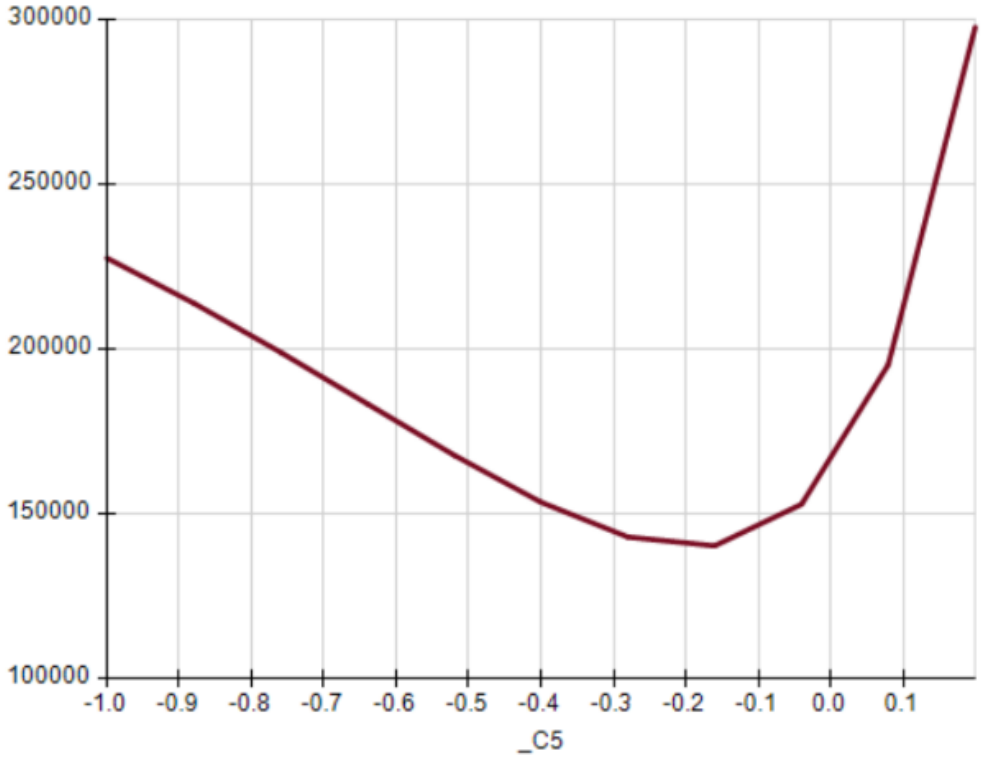

732

733

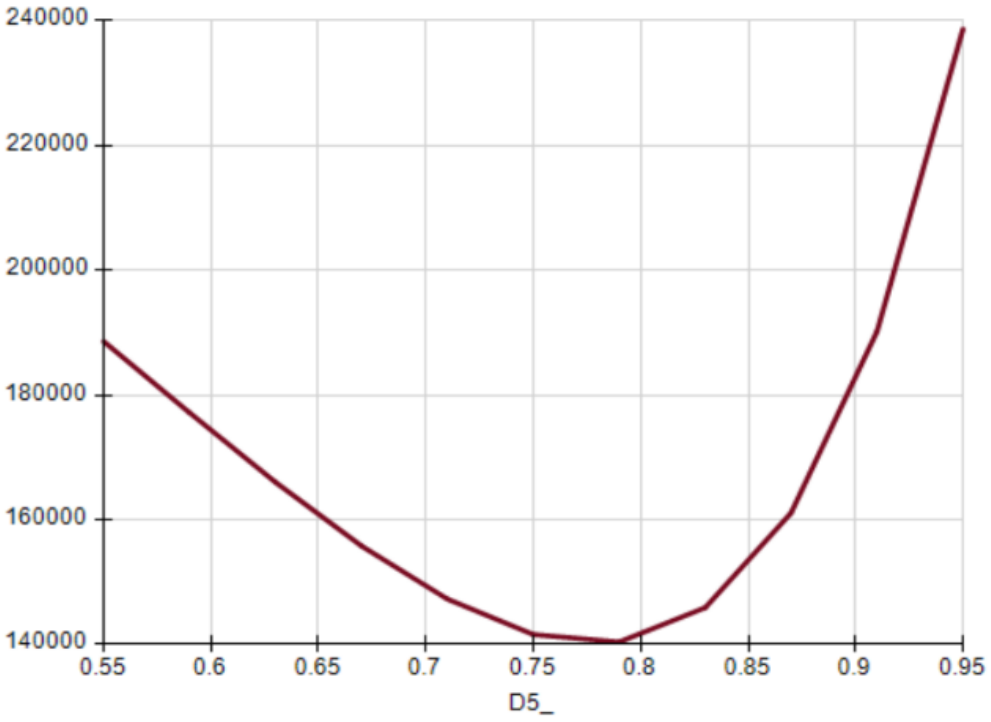

734

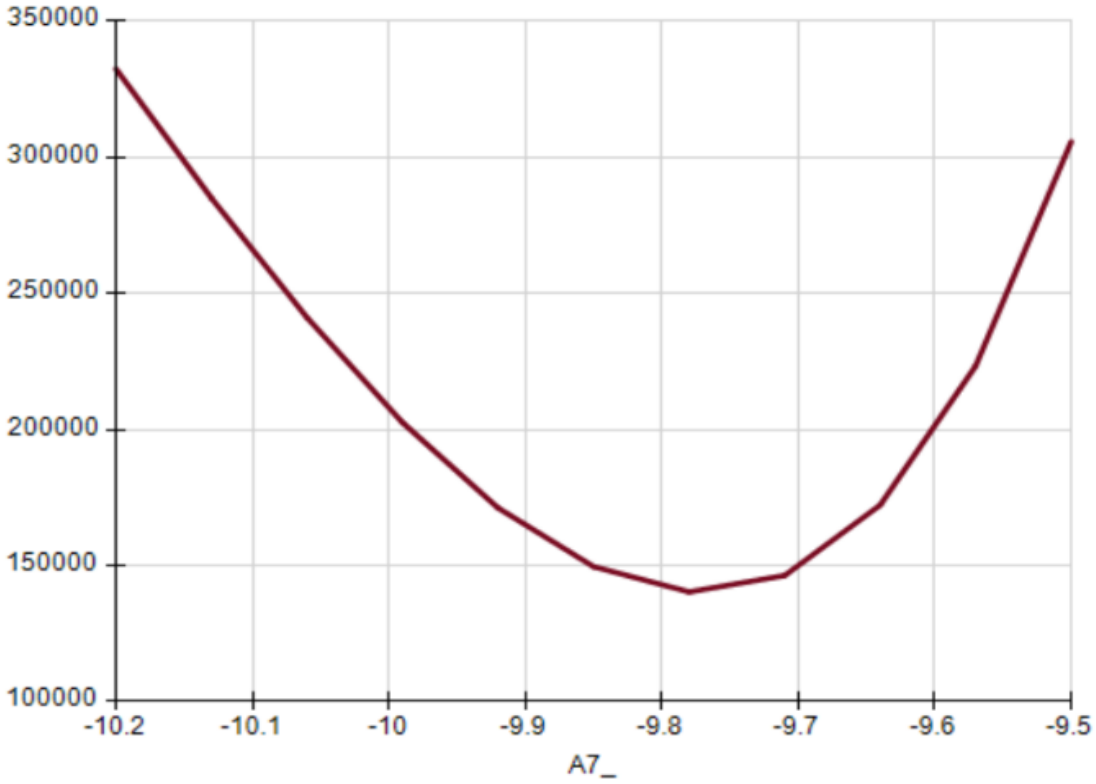
350000
300000
250000
200000
150000
100000
-10.2
-10.1
-10
-9.9
-9.8
-9.7
-9.6
-9.5
A7_

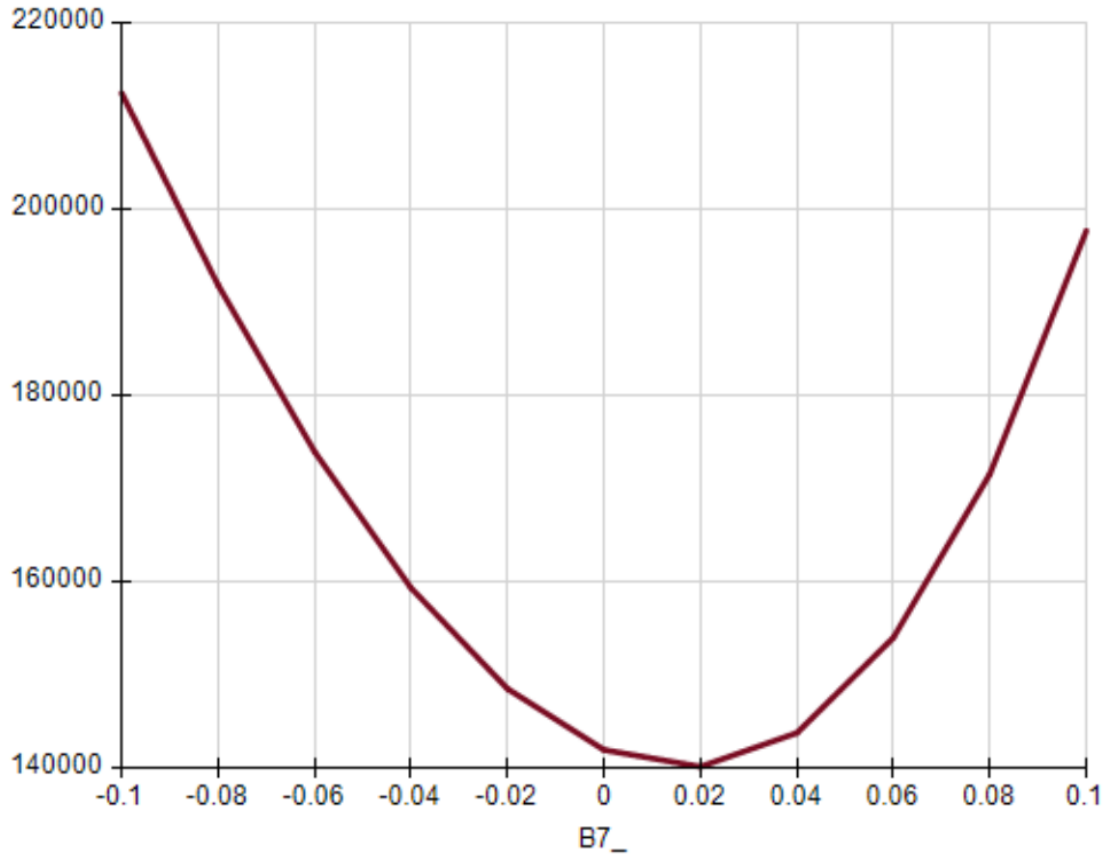
220000
200000
180000
160000
140000
-0.1
-0.08
-0.06
-0.04
-0.02
0
0.02
0.04
0.06
0.08
0.1
B7_

748

749

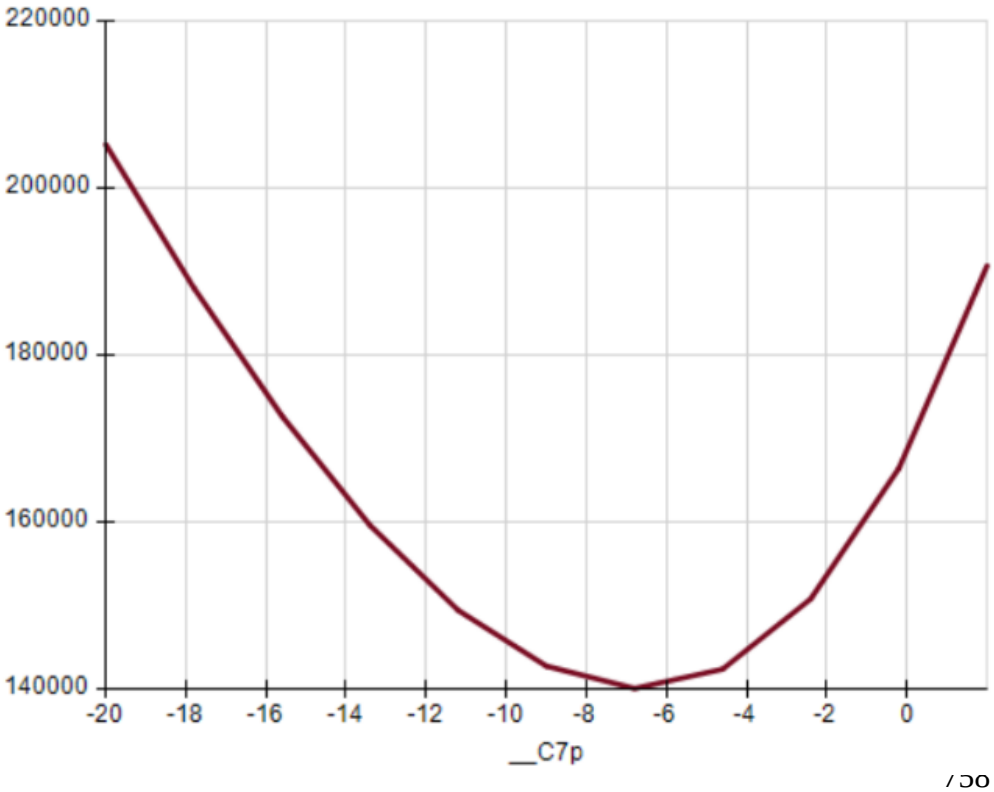
220000
200000
180000
160000
140000
-20
-18
-16
-14
-12
-10
-8
-6
-4
-2
0
__C7p

758

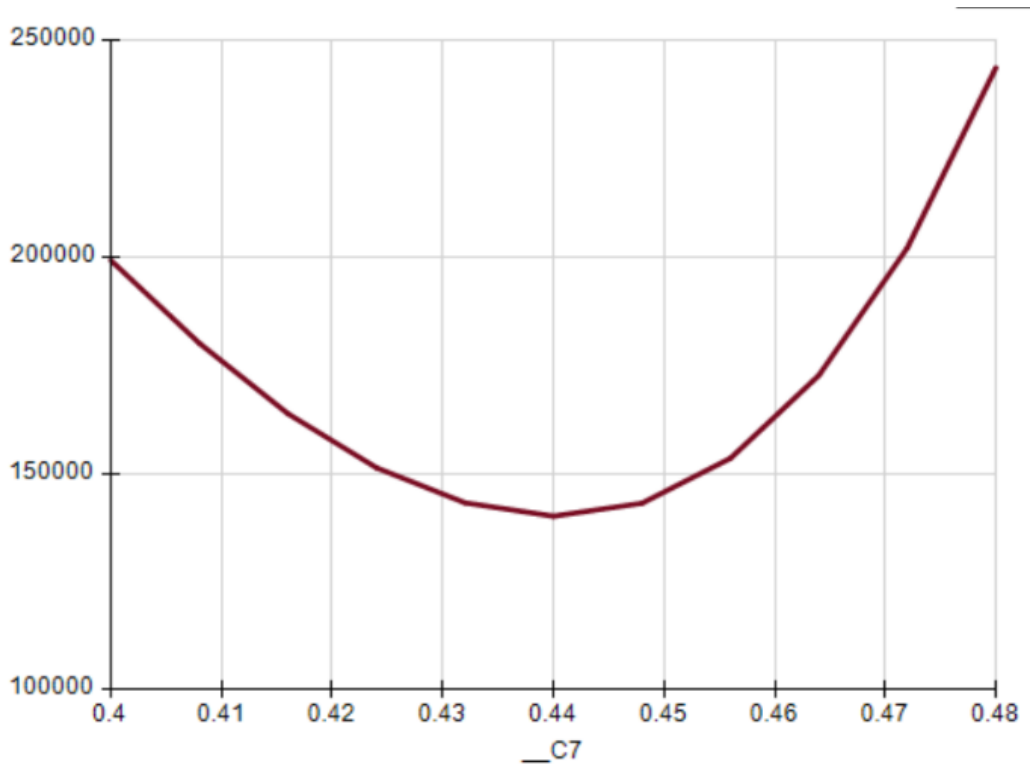

Figure S2: Example of sensitivity tests on some regressed parameters. The vertical axis is the Soptim value. Soptim values < 180,000 define the acceptable range of regressed parameters.

Supplementary references:

Jiang, G-R, Li, Y-X, Liu, Y., 2011. Calculation of hydrogen solubility in molten alloys. Trans. Nonferrous Met. Soc. China 21, 1130-1135.

778 Lob, A., Senk, D., Hallstedt, B., 2011. Determination of Hydrogen Solubility in Fe–Mn–C
779 Melts. Steel Research Int. 82, No. 2. DOI: 10.1002/srin.201000262

780 Wang, C., Hirama, J., Nagasaka, T., Ban-Ya, S., 1991. Phase equilibria of liquid Fe–S–C
781 ternary. ISIJ International 11, 1292–1299.

782